Received: 30 January 2024 | Revised: 6 March 2024 | Accepted: 7 March 2024

DOI: 10.1002/psc.3599

RESEARCH ARTICLE

Journal of PeptideScience WILEY

Impact of glycan nature on structure and viscoelastic properties of glycopeptide hydrogels

Jonas Proksch[1] | Marlene C. S. Dal Colle[1,2] | Frederick Heinz[1] | Robert F. Schmidt[3] | Jacqueline Gottwald[4] | Martina Delbianco[2] | Bettina G. Keller[3] | Michael Gradzielski[3] | Ulrike Alexiev[4] | Beate Koksch[1]

[1]Institute of Chemistry and Biochemistry, Freie Universität Berlin, Berlin, Germany

[2]Department of Biomolecular Systems, Max Planck Institute of Colloids and Interfaces, Potsdam, Germany

[3]Stranski-Laboratorium für Physikalische und Theoretische Chemie, Institut für Chemie, Technische Universität Berlin, Berlin, Germany

[4]Department of Physics, Freie Universität Berlin, Berlin, Germany

Correspondence
Beate Koksch, Institute of Chemistry and Biochemistry, Freie Universität Berlin, Arnimallee 20-22, 14195 Berlin, Germany.
Email: beate.koksch@fu-berlin.de

Funding information
Deutsche Forschungsgemeinschaft, Grant/Award Number: Project ID 431232613 - SFB 1449; Freie Universität Berlin; Max Planck Society

Mucus is a complex biological hydrogel that acts as a barrier for almost everything entering or exiting the body. It is therefore of emerging interest for biomedical and pharmaceutical applications. Besides water, the most abundant components are the large and densely glycosylated mucins, glycoproteins of up to 20 MDa and carbohydrate content of up to 80 wt%. Here, we designed and explored a library of glycosylated peptides to deconstruct the complexity of mucus. Using the well-characterized hFF03 coiled-coil system as a hydrogel-forming peptide scaffold, we systematically probed the contribution of single glycans to the secondary structure as well as the formation and viscoelastic properties of the resulting hydrogels. We show that glycan-decoration does not affect α-helix and coiled-coil formation while it alters gel stiffness. By using oscillatory macrorheology, dynamic light scattering microrheology, and fluorescence lifetime-based nanorheology, we characterized the glycopeptide materials over several length scales. Molecular simulations revealed that the glycosylated linker may extend into the solvent, but more frequently interacts with the peptide, thereby likely modifying the stability of the self-assembled fibers. This systematic study highlights the interplay between glycan structure and hydrogel properties and may guide the development of synthetic mucus mimetics.

KEYWORDS
glycopeptide library, mucus, peptide hydrogels, peptide self-assembly, rheology

1 | INTRODUCTION

Mucus is a biological hydrogel at the interface between the body and the environment. It lines every wet epithelial surface and forms a highly selective barrier. While it allows for the exchange of nutrients and gases, noxious agents, and pathogens are entrapped. Mucus also serves to hydrate the underlying mucosa and acts as a lubricant.[1] Moreover, it hosts a remarkably diverse microbial community essential to human health.[2] Primarily responsible for many of these properties are the major structural components of mucus, the mucins. Mucins are a class of over 20 mucin-type high molecular weight glycoproteins, all belonging to the *MUC* gene family. The mucin molecule is composed of a rigid and extended protein backbone with a variable number of tandem repeats rich in proline, threonine, and serine (PTS domains), as well as cysteine-rich regions at the two termini and between PTS domains.[3] The PTS domains are usually densely

O-glycosylated with branched oligosaccharide chains forming a structure that resembles a bottlebrush. The semi-flexible protein backbone and the highly hydrophilic nature of the *O*-glycans contribute to the biophysical properties of mucus. The hydrogel character of mucus is mainly arising from the entanglement of mucin fibers that form a three-dimensional network as well as non-covalent interactions and disulfide bonds. While the viscoelastic properties can vary drastically depending on the organ of origin and the state of health or disease, the storage modulus *G*' of healthy mucus is in the range of 1–10 Pa for probing frequencies above 1 Hz. The mesh size of mucus is also highly heterogeneous and can vary from 20 to 1800 nm across different organs.[4]

In order to understand this very complex material and its role in the pathways of many infectious and chronic diseases there is a need for artificial mucin-like systems that mimic some of the properties and functions of native mucus. Ribbeck et al have shown recently that single glycans are inhibitors of virulence in *Vibrio cholerae*.[5] Well-defined synthetic model systems that display single glycans can thus help identify such core structures and elucidate their role in the onset of disease, for example by performing binding studies with pathogens. It is however not trivial to mimic and investigate these intricate structures based on chemically synthesized materials and current research often relies on reconstituted mucins of animal origins. Commercially available mucins are for example bovine submaxillary mucin (BSM) or porcine gastric mucin (PGM).[6] All these samples differ largely in their molecular, mesoscopic, and macroscopic properties depending on the donor species and their state of health or disease.[7] Moreover, for commercial mucins the isolation procedure often changes the physicochemical properties irreversibly, leading to different characteristics and structures after rehydration of the mucin.[8,9] Hence, there is a great need for a chemically defined synthetic model mimicking key properties of mucus that would enable systematic studies based on reproducible (starting) conditions. Recently, different polymerization approaches have been used to mimic mucins and their hydrogels.[10,11] We chose to employ a peptide-based approach. The advantage that this system offers lies in its modularity, well-defined structure, and easy synthetic access. Through solid phase peptide synthesis (SPPS) access to well-defined structures is possible in a relatively short amount of time. This backbone can then be decorated with synthetic glycans obtained via chemical or chemoenzymatic syntheses. Such reductionist approaches were used before to investigate other complex biomaterials, such as amyloids.[12,13]

Prior work from our group focused on the defined presentation of glycans using self-assembling peptide scaffolds[14,15] and the functionalization of peptide hydrogels with cell adhesion motives and mannose[16]. Here we extend these systems to include decoration with mucin-relevant glycans and characterize hydrogel properties on different length scales, focusing on rheology. We used several experimental techniques to investigate the physicochemical features that characterize a mucus-inspired hydrogel over a range of length scales and how they change upon the introduction of single glycans. Oscillatory shear rheology is used to obtain macroscopic bulk properties, such as the storage (*G*') and loss modulus (*G*") associated with the elastic and viscous properties, respectively, on length scales from 0.1–10 mm. Dynamic light scattering (DLS) microrheology yields insight into the microstructural organization on length scales from 0.01–1 μm. By following the scattering of tracer particles, one can gain their mean squared displacement (MSD) and diffusion coefficient. Moreover, we used a recently established nanorheology technique that translates the fluorescence lifetime of a molecular rotor dye (FMR) into information about its immediate environment (<10 nm). This technique can thus give an idea of how small analytes move within the hydrogel. Finally, we aimed to bridge the gap between macro and nanorheology by DLS microrheology, which can give overlapping information with both of the other techniques. Additionally, we used molecular dynamics simulations to elucidate the dynamics and the structure of the glycosylated linker relative to the peptide.

2 | MATERIALS AND METHODS

2.1 | Preparation of peptide conjugate hydrogels

The synthesis of the glycan peptide conjugates can be divided into three parts. Firstly, the glycan building block was synthesized. Next, the peptide was synthesized using solid-phase peptide synthesis (SPPS). Lastly, the peptide, while still on-resin, was selectively deprotected at lysine residue 18, and the glycan was attached at this point.

2.1.1 | Synthesis of glycans

The glycans were synthesized according to published procedures either via automated glycan assembly (AGA)[17,18], solution phase synthesis,[19,20] or chemoenzymatic synthesis (for sialylated glycans)[21,22]. The structures carry an aminopentanol linker at the reducing end to be used for conjugation to the peptide. Details and analytical data can be found in section 1 of the supporting information.

2.1.2 | Synthesis of peptides

Peptides were synthesized by standard fluorenylmethoxycarbonyl (Fmoc) microwave-assisted SPPS according to established procedures.[16] For details, see section 2 of the supporting information.

2.1.3 | Glycan decoration of peptides

Conjugation of glycans to the peptide backbone followed a slightly modified protocol from Hellmund et al.[16] Briefly, after full-length synthesis, the Mmt-protected lysine residue at position 18 was deprotected and the freed ε-amino function was then converted into a carboxy function using glutaric anhydride. This was then activated with HATU/DIPEA and the respective glycan was coupled. Full

cleavage of the glycosylated peptides was achieved by treating the resin with a mixture of TFA, dichloromethane, TIPS, and water (50:45:2.5:2.5 v/v) for 3 × 30 min. Volatiles were evaporated and the peptides precipitated in cold diethyl ether, centrifuged, dissolved in water, and lyophilized. Purification was performed using preparative RP-HPLC. The obtained pure peptides inevitably yield trifluoroacetic acid anions, which were exchanged for chloride following common protocols.[16] For more exact procedures, refer to section 3 of the supporting information.

2.2 | Sample preparation

Purified peptide HCl salts were dissolved in 1,1,1,3,3,3-hexafluoroisopropanol (HFIP) at roughly 1 mg per 100 µl and sonicated for 15 minutes. An aliquot of the stock solution was evaporated in a gentle stream of nitrogen gas and the resulting peptide film dissolved in 1 ml of Dulbecco's phosphate-buffered saline (DPBS) containing 6 M guanidine hydrochloride. The absorbance of this solution at 320 nm was measured with a Varian Cary 50 photometer (Varian Medical Systems, Palo Alto, CA, USA). The concentration was then calculated using a calibration curve of dipeptide H-Abz-Gly-OH (see Figure S1).

From the HFIP peptide stock solutions of known concentration appropriate amounts were then evaporated using a gentle flow of nitrogen gas, and the resulting peptide residue was then dissolved as described in the respective experiment section.

2.3 | Circular dichroism spectroscopy

Circular dichroism (CD) spectra of hydrogel samples were recorded using demountable Quartz Suprasil cuvettes (Hellma Analytics, Mühlheim, Germany) with a path length of 0.1 mm. Measurements were performed at 37°C and a mean of three measurements was taken. Spectra were background-corrected by subtraction of solvent/buffer spectra at 37°C and normalized by path length, molar concentration, and the number of amide bonds.

Samples were prepared by dissolving peptides in either DPBS (w/o Ca^{2+}, Mg^{2+}, Sigma) or water for pH-dependent experiments. In the case of water, pH was adjusted to the desired pH by the addition of 1 M aqueous NaOH or HCl and the remaining volume until the desired concentration was filled up using 150 mM NaCl solution to account for ion strength. Samples were vortexed for 10 s and incubated for 16 h at room temperature (19–21°C).

2.4 | Rheology

2.4.1 | Macrorheology

All macrorheological measurements were performed on an Anton Paar MCR 502 WESP temperature-controlled rheometer in strain-imposed mode at 37°C. A chromium oxide-coated cone-plate measurement system was used with a diameter of 25 mm, a cone truncation (gap width) of 48 µm, and a cone angle of 1°. The temperature was set using a Peltier measuring system combined with a Peltier hood to ensure a minimized temperature gradient throughout the sample. For each measurement, 120 µl of sample was loaded onto the plate, the cone was lowered slowly and any excess sample was trimmed before starting the measurement.

In a preliminary amplitude sweep (AS), the strain amplitude γ_0 was varied between 0.1 and 10% at a constant frequency of 6.3 rad/s to determine the linear viscoelastic regime. For the frequency sweeps, the strain amplitude was kept fixed at 5% (value determined from AS) and the oscillation frequency varied between 0.05 and 50 Hz, which corresponds to 0.314 and 314 rad/s. For each sample, the frequency was first varied in increasing and then in decreasing order to check for hysteresis effects. Since no systematic hysteresis effects were observed, only the increasing frequency data are considered below. At very high frequencies, artifacts can occur, leading to unrealistic values for G' and G''. Therefore, only frequencies $\omega \leq 52.4$ rad/s are considered.

In addition, continuous shear experiments were performed, where the shear rate was varied between 0.01 and 100 s^{-1}, first in increasing and then in decreasing order. New data points are created when the measured viscosity is constant within a 1% error for 2 s. This means that the overall measurement time varies from sample to sample.

Samples were prepared by dissolving peptides in either DPBS (w/o Ca^{2+}, Mg^{2+}, Sigma) or water. pH was adjusted by the addition of 1 M aqueous NaOH or HCl and the remaining volume until the desired concentration filled up using 150 mM NaCl solution to account for ion strength. Samples were vortexed for 10 s and incubated for 16 h at room temperature (19–21°C).

2.4.2 | DLS-microrheology

DLS measurements were performed on a Litesizer 500 instrument from Anton Paar (Graz, Austria), equipped with a 40 mW semiconductor laser diode with a wavelength of $\lambda = 658$ nm at a fixed scattering angle of $\theta = 175°$. Using the refractive index of DPBS buffer $n = 1.3318$, the magnitude of the scattering vector scattering vector is $q = 4\pi n/\lambda \sin(\theta/2) = 0.025\text{nm}^{-1}$. A 3 × 3 mm low-volume quartz cuvette was used at a constant temperature of 25°C. Three separate 30 min measurements were performed and averaged. The intensity-intensity autocorrelation function $g^{(2)}(\tau)$ can be related to the mean-squared displacement $\langle \Delta r^2(\tau) \rangle$ (MSD) of the tracer particles through the intermediate scattering function[23]

$$g^{(1)}(\tau) = exp\left(\frac{-q^2\langle \Delta r^2(\tau)\rangle}{6}\right) \quad (1)$$

Assuming that the sample is ergodic, $g^{(1)}(\tau)$ is related to $g^{(2)}(\tau)$ through the Siegert relation[24,25]

$$g^{(2)}(\tau) = 1 + \beta |g^{(1)}(\tau)|^2 \quad (2)$$

where $\beta = g^{(2)}(\tau \to 0)$ is determined by fitting a stretched exponential to $g^{(2)}(\tau)$ for 8.8×10^{-7} s < τ < 1.41×10^{-5} s. Inaccuracies in the determination of β can influence the y-intercept of the MSD. Since by definition, $\langle \Delta r^2(\tau = 0) \rangle = 0$, we perform a linear fit of the MSD in the range $10^{-6} < \tau < 5 \times 10^{-6}$ s and subtract the y-intercept. The MSD of tracer particles embedded in a viscoelastic fluid can be converted to the complex modulus $G^*(\omega)$ using the generalized Stokes-Einstein equation[26,27]

$$G^*(\omega) = \frac{kT}{\pi a i \omega \mathcal{F}_u\{\langle \Delta r^2(\tau) \rangle\}} \quad (3)$$

where a is the tracer particle radius, i is the imaginary unit, and $\mathcal{F}_u\{\langle \Delta r^2(\tau) \rangle$ denotes the unilateral Fourier transform of the MSD. Instead of performing a numerical Fourier transform, we adopt the method introduced by Mason et al., where the MSD is described by a local power-law followed by an analytical Fourier transformation.[28,29] The power law exponent $\alpha(\omega)$ is determined from the logarithmic time derivative of the MSD:

$$\alpha(\omega = 1/\tau) = \frac{\partial ln \langle \Delta r^2(\tau) \rangle}{\partial ln \tau} \quad (4)$$

where we have used that the frequency is the inverse of the lag time. In viscoelastic fluids, 0 < α < 1 (0 corresponds to a purely elastic solid and 1 corresponds to a purely viscous liquid). Analytical Fourier transform of the local power law, together with Equation 7 yields

$$G'(\omega) = G(\omega) cos[\pi\alpha(\omega)/2] \quad (5)$$

$$G''(\omega) = G(\omega) sin[\pi\alpha(\omega)/2] \quad (6)$$

where

$$G(\omega) = \frac{kT}{\pi a \langle \Delta r^2(1/\omega) \rangle \Gamma[1 + \alpha(\omega)]} \quad (7)$$

Here, $\Gamma(z) = \int_0^\infty x^{z-1} e^{-x} dx$ is the Gamma function.

Samples were prepared by dissolving peptides in a suspension of Cy3 labeled polystyrene beads (Nanocs, hydrodynamic diameter = 216.9 nm) in DPBS (w/o Ca^{2+}, Mg^{2+}, Sigma). Samples were vortexed for 10 s and incubated for 16 h at room temperature (19–21°C).

2.5 | Spectroscopy

2.5.1 | Time-resolved fluorescence spectroscopy in FLIM mode

The fluorescence lifetime curves of Cy3 (sulfo-Cyanine 3 maleimide [Lumiprobe, Germany]) in the peptide hydrogel and in different sucrose/water mixtures were recorded in a home-built setup combining time-correlated single photon counting (TCSPC) and confocal laser scanning microscopy as previously described[30,31] to allow the measurement of small samples of 25–50 µl hydrogel. The setup consists of an inverted microscope (IX71, Olympus, Shinjuku, Tokyo, Japan), a tunable ps-supercontinuum white light laser (SuperK Extreme EXU-3, NKT Photonics, Birkerød, Denmark), a confocal scanning unit (DCS120, Becker & Hickl, Germany), a hybrid PMT detector (HPM-100-40, Becker & Hickl, Germany), and a TCSPC-module (SPC150, Becker & Hickl, Germany). FLIM images were recorded by the SPCM software (Becker & Hickl, Germany) using a 60× objective (water, UPLSAPO60XW, Olympus, Japan), resulting in a total field of view with 300 µm side length. An acousto-optical tunable filter (SELECT UV–VIS, NKT Photonics, Denmark) was used to select the fluorescence excitation wavelengths from the white light laser beam. The laser repetition rate was set to 19.5 MHz. Cy3 was excited at 530 nm and the fluorescence emission was spectrally selected by a long-pass filter (> 545 nm, Chroma, Rockingham, USA). A notch filter (Semrock, USA) removed the residual scattered excitation light. The TCSPC-module sorts the detected fluorescence photons into 1,024 time channels with a channel width of 19.97 ps. The instrument response function (IRF) of the system was less than 100 ps (FWHM). To analyze the fluorescence decay traces, the decay histograms from all pixels in the FLIM image were summed up. Subsequently, the fluorescence decay curve was fitted by a multi-exponential model function after deconvolution using a calculated IRF

$$I(t) = \sum_i^n \alpha_i e^{-t/\tau_i}, \quad (8)$$

with n the total number of decay components, α_i the amplitude, and τ_I the fluorescence lifetime of the i-th component[32,33]. The population-weighted mean fluorescence lifetime τ_{mean} was calculated by

$$\tau_{mean} = \sum_i^n \beta_i \tau_i, \quad (9)$$

with β_i being the fractional amplitude (population amplitude) of the i-th component with

$$\beta_i = \frac{\alpha_i \tau_i}{\sum_i^n \alpha_i \tau_i}. \quad (10)$$

2.5.2 | Viscosity dependence of Cy3 fluorescence decay traces

Cy3 was investigated by time-resolved fluorescence spectroscopy in sucrose/water mixtures ranging from 0% to 70% (w/w) sucrose. The obtained fluorescence decay traces were fitted by Equation 8 and the mean fluorescence lifetimes were calculated by Equation 9. The viscosity dependence was analyzed as previously described for a

cyanine 3 dye[30]. Briefly, the viscosity values were taken from ref.[34] at the different sucrose concentrations. The mean fluorescence lifetimes as a function of viscosity were evaluated by an extended Förster–Hoffmann equation, which includes a temperature-dependent activation energy for dye isomerization:

$$\overline{\tau}_{pop} = \left(\frac{1}{C\eta^{\alpha} + \frac{1}{A_{max}}} \cdot e^{-\frac{E_a}{kT}} + k_f + k_x \right)^{-1}. \quad (11)$$

C is a constant and $1/A_{max}$ indicates that τ does not go to zero at zero viscosity, k_f and k_x are the rate of fluorescence and all other non-radiative rates, respectively, from the excited to the ground state[30,35].

2.5.3 | Hydrogel preparation for nanoviscosity studies using Cy3

Peptide was dissolved in 50 µl aliquots at a concentration of 0.5% (w/v) in DPBS (w/o Ca^{2+}, Mg^{2+}, Sigma), which included 0.5 µM Cy3, vortexed for ten seconds, gently mixed by pipetting and again vortexed for ten seconds. After 1–2 h the solution was again carefully mixed by pipetting to allow homogeneous hydrogel formation and was used for Cy3 fluorescence lifetime measurements the following day. To follow the viscosity increase during peptide hydrogel formation, we measured the Cy3 fluorescence lifetime at different time delays after initial mixing with buffer.

2.6 | Molecular dynamics simulations

2.6.1 | Simulations

The initial coiled-coil structure was built with the sequence LKKELAA-LKKELAA-LKKELAA-LKKEL using the web tool CCBuilder2.0 by Derek Woolfson.[36] Lysine residues and amino group of the *ortho* aminobenzoic acid are protonated (charge+1), glutamate residues and the C-terminus are deprotonated (charge −1), corresponding to the expected protonation at pH 7. A single coiled-coil dimer has a total charge of +8. The *ortho* aminobenzoic acid at the N-terminus, the anhydride linker, and the C5 chain were added manually with Pymol. The corresponding force field parameters were calculated with AmberTools[37], with the gas charge calculation method. The glycans α-mannose, β-glucose, β-galactose, and their force field parameters were added with doGlycans[38]. 32 coiled-coil dimers of α--mannose-hFF03, β-glucose-hFF03 or β-galactose-hFF03 were solvated in TiP4P water with 0.1 M NaCl in a cubic box with 20 nm box length, corresponding to roughly a 4% polymer mass fraction. A total of 256 Cl^- anions were added to generate a neutral simulation box.

MD simulations were carried out with Gromacs2021 + CUDA on the Curta cluster system[39] with the Amber99SB-ILDN force field[40]. After energy minimization and relaxation in the NVT and NPT ensemble, the simulations are carried out in the NPT ensemble. The temperature was maintained at T = 300 K using the velocity-rescale thermostat with a coupling constant of 0.1 ps. The pressure was maintained at 1 bar using the Parinello-Rahman barostat with a coupling constant of 2 ps. The simulation uses a leap frog integrator with 2 fs per step and periodic boundary conditions in all three spatial directions. Covalent bonds to hydrogen atoms were constraint using the LINCS algorithm. Coordinates were written to file every 20 ps. A simulation of 50 ns length was conducted for each of the three systems.

The force field and all input files for the simulations are available via the code repository: https://github.com/bkellerlab/hFF03_hydrogels.

2.6.2 | Analysis

To analyze the relative positions of the glycans to the coiled-coil backbone we consider the backbone of a single coiled-coil to be linear. This allows the use of trigonometry to specify the position of the glycan. First, we create a backbone vector $\vec{v}$ from the N-terminus to the C-terminus. To obtain a vector going through the center of the coiled-coil, we use the average of the C_α atoms for both α-helices of the coiled-coil. We specifically use the C_α atoms of the first and last lysine since these are always oriented toward the center of the coiled-coil (lysine zipper). For the glycan, we use the center of mass averaged position of the entire glycan (without the C5 tail) called $\vec{G}$. We can now calculate the distance d of the glycan toward the coiled-coil with:

$$d = \frac{\left|\vec{G} \times \vec{v}\right|}{\left|\vec{v}\right|} \quad (12)$$

For the position along the coiled-coil, we use the relative position r since the length slightly varies by simulation frame and it is easier to see the length of the original coiled-coil. Due to the linker and the C5 chain, the glycan can extend beyond the coiled-coil in both directions. 0% and 100% are the N- and C-terminus, respectively (without the chromophore). The relative position can be calculated with:

$$r = \frac{\vec{G} \cdot \left|\vec{v}\right|}{\left|\vec{v}\right|} 100\% \quad (13)$$

2.7 | Cryo-transmission electron microscopy

Cryo-transmission electron microscopy (cryo-TEM) was measured of 0.1% (w/v) peptide hydrogel samples that were prepared as described above. Peptide gel aliquots of 5 µl were applied on pre-cleaned 200 mesh perforated carbon film-covered microscopical grids (R1/4 batch of Quantifoil, MicroTools GmbH, Jena, Germany). The grids were cleaned with chloroform and hydrophilized by 60 seconds glow discharging at 8 W in a BALTEC MED 020 device (Leica Microsystems, Wetzlar, Germany). The samples were blotted and vitrified using

an FEI Vitrobot Mark IV and liquid ethane as a cryogen. After transferral to a FEI TALOS ARCTICA electron microscope equipped a with high-brightness field-emission gun (XFEG) operating at an acceleration voltage of 200 kV, micrographs were acquired on a FEI Falcon 3 direct electron detector (Thermo Fisher Scientific Inc., Waltham, Massachusetts, USA) using a 70 µm objective aperture at a nominal magnification of 28,000 or 36,000, corresponding to a calibrated pixel size of 3.69 or 2.97 Å/pixel, respectively.

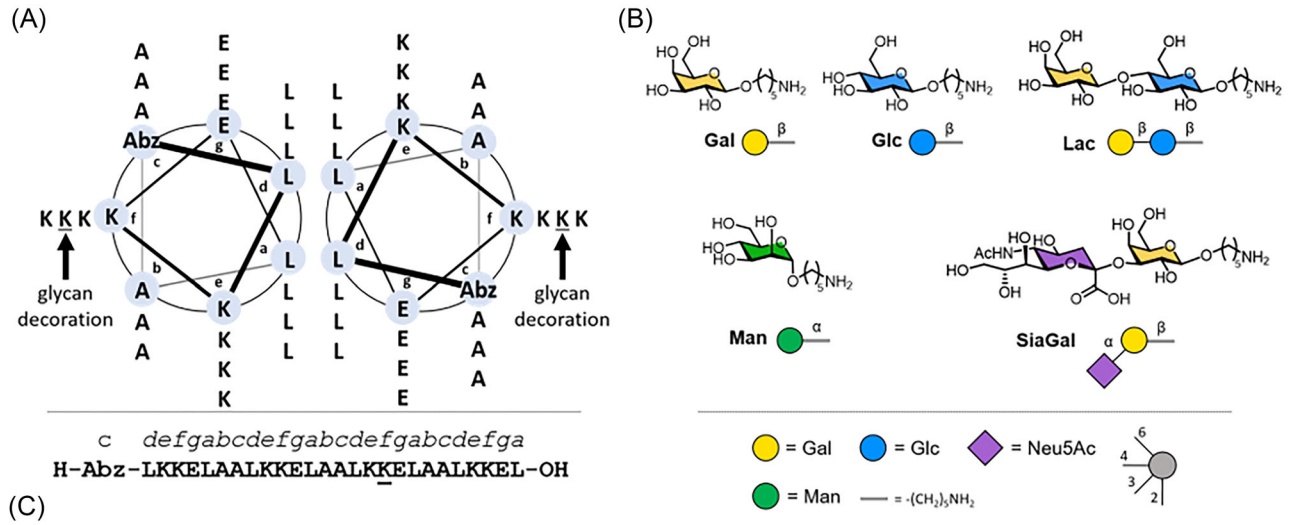

(C)

	Experiment	Output	Interpretation	Length scale
Macrorheology	Oscillatory shear rheology 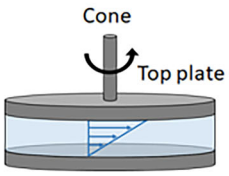	Storage modulus G'(ω), Loss modulus G''(ω), Plateau modulus G_0	Bulk mechanical properties	0.1-10 mm
Microrheology	Dynamic light scattering 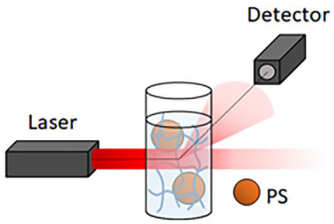	Mean squared displacement (MSD), Diffusion coefficients	Microstructural organisation	0.01-1 µm
Nanorheology	FMR/FLIM spectroscopy 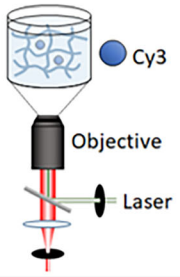	Nanoviscosity, time dependent nanoviscosity	Biochemical interaction and transport	<10 nm

FIGURE 1 a) Helical wheel projection and sequence of the hFF03 peptide; b) carbohydrate motifs used for decoration of the peptide backbone; c) overview of rheological techniques and their readouts for comparing the influence of glycans on the physicochemical properties of glycopeptide hydrogels at different length scales. Table adapted with permission from reference 9.

3 | RESULTS AND DISCUSSION

3.1 | Design of the glycopeptide library

The coiled-coil structure is widely observed in nature and has drawn substantial interest due to its clear sequence-to-structure relationship and ease of tunability.[14,15,41,42] It has been used to create and study higher-order assemblies[43] and for a multitude of biomedical applications[44–47]. The hFF03 (hydrogelating fiber-forming) peptide was developed in our group and used as a tuneable extracellular matrix mimic by decoration with cell adhesion motives or carbohydrate ligands.[16] We chose to use this scaffold for its synthetic accessibility and straightforward decoration leading to defined glycan-peptide conjugates.

hFF03 is a 26-residue peptide that forms α-helical coiled-coil dimers of 4 nm length (Figure 1a). Its design follows a well-known heptad repeat pattern, denoted *abcdefg*, where positions *a* and *d* are hydrophobic residues (leucine in this case) forming a hydrophobic core in the dimer. Positions *e* and *g* are occupied by oppositely charged residues lysine and glutamic acid, respectively, further stabilizing the dimer via electrostatic interactions. Solvent-exposed positions *b* and *c* are both occupied by alanine to induce weak hydrophobic interactions, they are critical for gel formation.[48] Position *f* is occupied by lysine to increase the overall charge and solubility of the peptide and to allow for facile functionalization.[16] The coiled-coil dimers subsequently self-assemble into fibrils via dimer-to-dimer contacts in which the N-terminus of one coiled-coil dimer forms a network of salt-bridges and hydrogen bonds to the C-terminus of an adjacent coiled-coil dimer. The stability of this dimer-to-dimer contact significantly influences the viscoelastic properties of the hydrogel.[49] In this study, we used *ortho*-aminobenzoic acid as an N-terminal label to determine exact peptide concentrations via UV/vis absorption spectroscopy (see section 2.2.3 of the supporting information). The fibrils formed by this system are highly dynamic with a persistence length of approximately 10 nm and a diameter of approximately 2.6 nm.[16]

This well-characterized system is suitable for studying the contribution of conjugated single components, such as monosaccharides, to the viscoelastic properties of the hydrogel. Therefore, this peptide backbone was systematically decorated with different single glycans (Figure 1b), and the properties of the resulting hydrogels were studied under different conditions. Lysine residue 18 was selected for decoration because it resides in the central heptad of the helix and is located in a solvent exposed *f* position. Earlier work has shown that it can be readily functionalized without impeding self-assembly.[16] The saccharides we chose (galactose, sialylated galactose) were derived from glycan motives found in native mucins (MUC5AC, MUC5B, MUC2)[50] and complemented by other glycan motives of interest (glucose, mannose, lactose) for a systematic study of the structure–property relationship.

3.2 | Synthesis

Peptides were synthesized using Fmoc-SPPS and remained attached to the solid support. Glycans were synthesized according to literature reports[17–21] and coupled to the peptide on-resin. After cleavage from the solid support and HPLC purification, the anions were exchanged from trifluoroacetate to chloride.

3.3 | Structural analysis

All glycopeptides were studied at different concentrations by means of circular dichroism (CD) spectroscopy. CD spectra at 0.1% (w/v) exhibit characteristic signals for α-helical structures, namely an ellipticity maximum at 195 nm and two minima, at 208 nm and 222 nm (Figure 2a).

At 0.5% (w/v) (Figure 2b), the maximum attenuates while the average intensity ratio of the two minima ($\theta_{222\ nm}/\theta_{208\ nm}$) shifts from 1.22 ± 0.11 toward 2.21 ± 0.35. This behavior has been attributed to the formation of higher-order helical structures[51] and is also in accordance

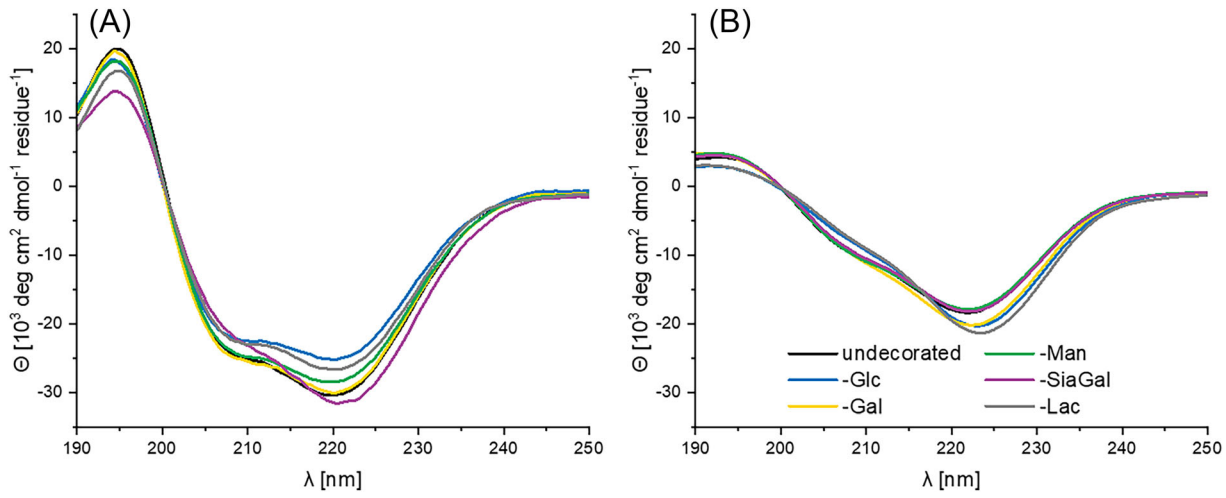

FIGURE 2 CD spectra of glycan-decorated peptides at 0.1% (w/v) (a) and 0.5% (w/v) (b) in DPBS recorded at pH 4 and 37°C.

with structural findings on the parent system hFF03[16]. Variations between the differently decorated peptides are minimal. It seems that α-helix and fiber formation occur regardless of the introduced glycan. This is in line with the finding that the assembly occurs via contact between the C-terminus and the N-terminus of the coiled-coils.[49]

Furthermore, the secondary structure of 0.5% (w/v) undecorated backbone hFF03 was evaluated at different pH values. As can be seen from Figure 3, the CD spectra are very similar, suggesting that the secondary structure is not perturbed by changes in pH. While the curve intensity is less pronounced at pH extremes (3.4 and 11.4) the curve shape remains unchanged meaning that the coiled-coils still assemble. From the generally higher intensity as compared to buffered conditions (Figure 2b) it can be concluded that helicity is stronger in unbuffered conditions.

Overall, CD experiments show that the hFF03-based coiled-coil motif is robust to the incorporation of single glycans and change of pH. At higher concentrations, CD indicates the formation of superstructures.

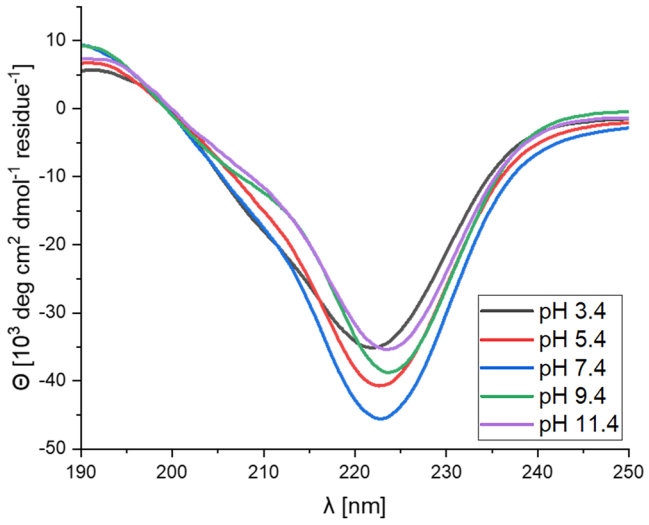

FIGURE 3 CD spectra of 0.5% (w/v) hFF03 at different pH values, recorded at 37°C. Samples were prepared in water + 150 mM NaCl and pH was adjusted using 1 M NaOH and HCl.

3.4 | Cryo-transmission electron microscopy (cryo-TEM)

The morphology of the decorated peptides was investigated by cryo-TEM. Solutions of 0.5% (w/v) of hFF03-Man and hFF03-SiaGal were prepared as described above and then diluted to 0.05% (w/v) using DPBS since the fiber density was too high to obtain meaningful micrographs otherwise. As can be seen from Figure 4, both hydrogels exhibit a network of extended fibers of about 3 nm diameter.

This morphology is also described for the undecorated parent peptide hFF03[16] and we therefore conclude that fiber formation is not altered by glycan decoration.

3.5 | Simulations (MD)

We conducted MD simulations of α-mannose-hFF03, β-galactose-hFF03, and β-glucose-hFF03 in explicit water to examine the structure and dynamics of the glycosylated linker. The glycans are connected through an extended linker to lysine at position 18, i.e., toward the C-terminus of the coiled-coil. Due to the length of the linker, the glycan can reach up to 4 nm into the solvent (Figure 5 A-C). Although this extension is significant, especially when considering that the coiled-coil's length is 4 nm, it is not enough to span the mesh sizes, which are around 50 nm in the undecorated hFF03[49] and up to around 80 nm in the glycosylated hFF03 (Table 1) as determined from macrorheology. The glycosylated linker in β-galactose-hFF03 (Figure 5 B) extends slightly further and more frequently into the solvent than in the other two simulated systems.

Overall, however, the extended conformation of the linker is a minor conformation. In the vast majority of the linker conformations, the glycans form interactions with the coiled-coil peptide. For example, they intercalate between two lysine side chains (Figure 5 E). This conformation is characterized by a relative position of 50–75% along the coiled-coil axis and a distance of around 1 nm from the axis and is particularly frequently populated in β-glucose-hFF03 (Figure 5 C).

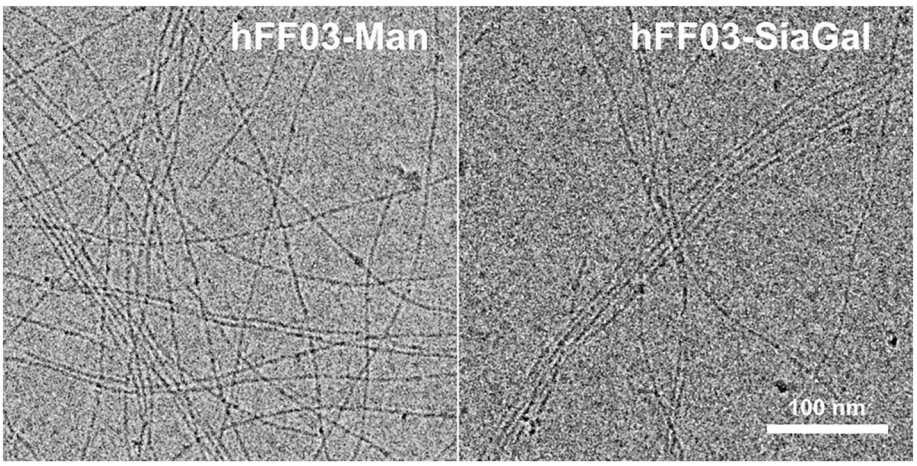

FIGURE 4 Cryo-transmission electron microscopy (cryo-TEM) images of 0.05% (w/v) peptide hydrogels, Man-decorated (left), and SiaGal-decorated (right). The scale bar denotes 100 nm.

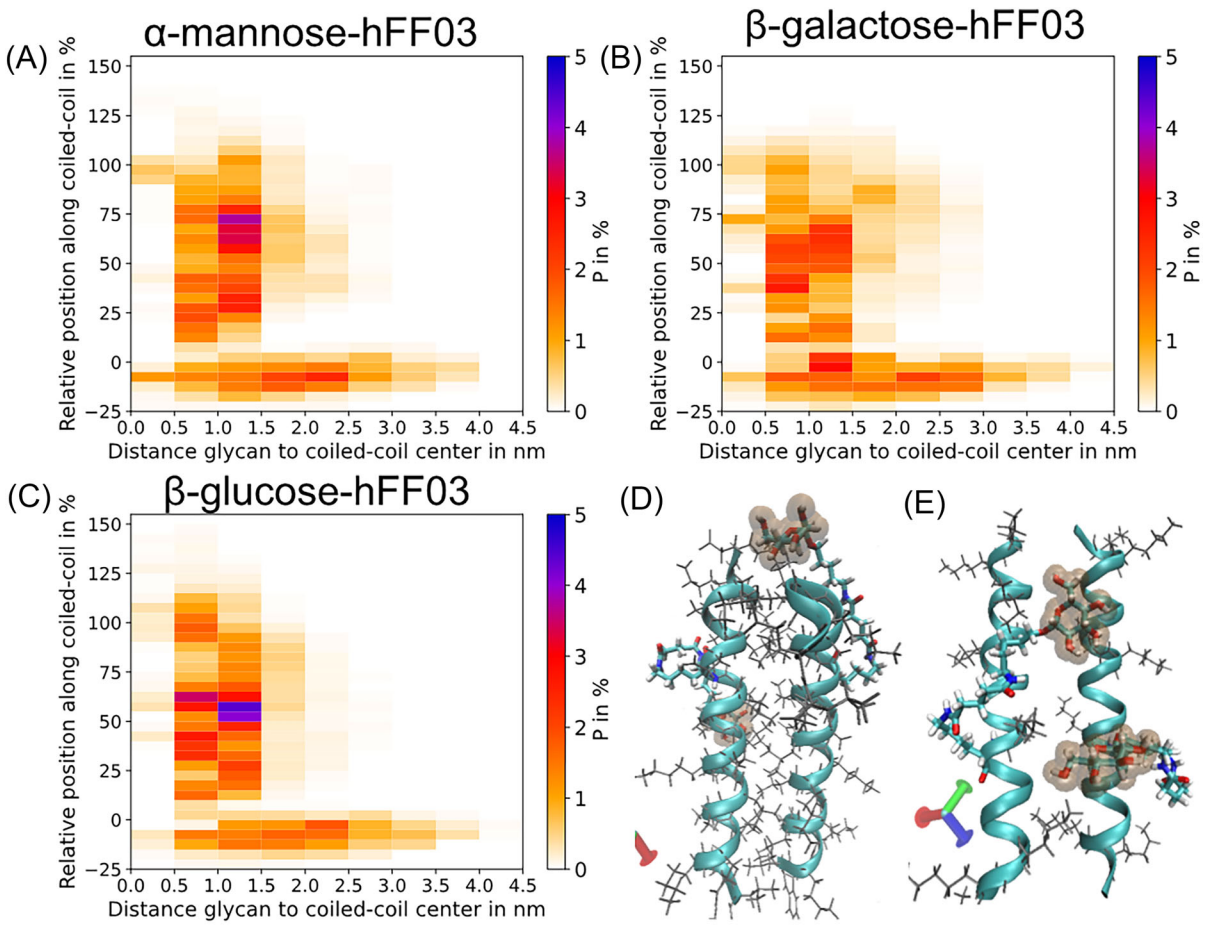

FIGURE 5 A-C: 2D histogram of the relative positions of the glycan toward its coiled-coil with α-mannose-hFF03 (A), β-galactose-hFF03 (B) and β-glucose-hFF03 (C). The color denotes the occurrence rate over all coiled-coils and simulation time. D and E show a single coiled-coil with the glycan highlighted to demonstrate the common configurations. D: the glycan is on top of the C-terminus. E: the glycan is nestled between two lysine sidechains.

The linker can also extend up to the C-terminus of the coiled-coil peptide, where the glycan forms a stable interaction with the terminal residues. This conformation is characterized by a relative position of 100% along the coiled-coil axis and a distance less than 1 nm from the axis. This conformation likely competes with the self-assembly of the coiled-coils into fibrils, which are stabilized by a salt-bridge network between the C-terminus and the N-terminus of consecutive coiled-coils.[49] Thus, the structure and dynamics of the linker may interfere with the hydrogelation process, and shortening the linker might stabilize the hydrogels.

3.6 | Viscoelastic properties

3.6.1 | Macrorheology

The rheological properties of 0.5% (w/v) solutions of peptide, decorated with various glycans, were studied by means of oscillatory shear rheology. In oscillatory shear rheology, samples are subjected to an oscillating shear strain, which yields the storage modulus G' (elastic response) and the loss modulus G'' (viscous response) as a function of frequency. The frequency sweep results are shown in Figure 6.

All peptide solutions show viscoelastic properties, with values for G' and G'' ranging from around 0.1 to 30 Pa. For all glycan-decorated peptides, a decrease in the viscoelastic response is observed compared to the undecorated peptide. The undecorated peptide shows the strongest viscoelastic response and has typical gel-like behavior with $G' > G''$ over the whole frequency range. In chemically cross-linked hydrogels, G' and G'' typically show close to no frequency-dependence.[52] In contrast, our self-assembled peptide hydrogels, G' and G'' exhibit considerable frequency-dependence, especially at low frequencies, indicating that these are dynamic systems that rearrange and relax over long time scales. The solutions of the Man-, Lac-, and SiaGal-decorated peptides can still be considered soft hydrogels since G' dominates over most of the frequency range. Furthermore, especially for the undecorated and the Man-decorated system, we observe clearly non-parallel behavior for G' vs. G'' as a function of frequency. Here, the viscosity related G'' changes rather little as a function of frequency, while G' increases systematically toward higher frequency. This can be attributed to the fact that apparently, these systems

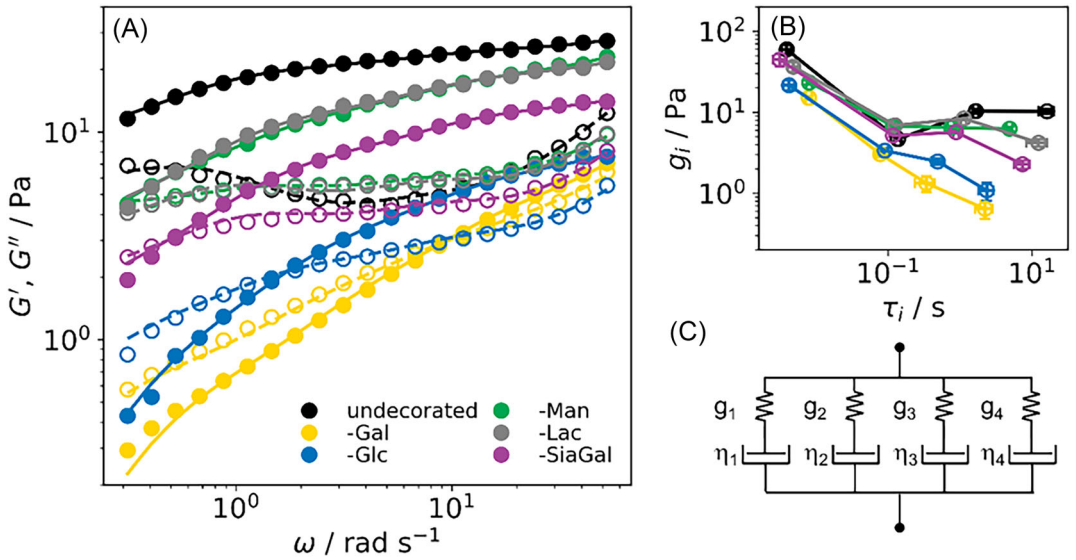

FIGURE 6 a) Frequency sweep data (filled symbols: *G'*, open symbols: *G''*) and generalized Maxwell model (GMM) fits (solid lines: *G'*, broken lines: *G''*) for solutions of the undecorated and decorated peptides (concentration always 0.5% w/v in DPBS at pH 4). b) Relaxation times and strengths as determined from GMM fits. c) Graphical representation of the generalized Maxwell model with 4 Maxwell elements connected in parallel. Experimental conditions: 37°C.

possess stress relaxation mechanisms that operate in this experimental frequency window, and accordingly, the elastic response still increases here for rising frequency.

To obtain further insight, the frequency sweep data were fitted with the generalized Maxwell model (GMM), also referred to as the Wiechert model.[53–55] This model is based on the idea that the overall viscoelastic relaxation is given by a superposition of individual exponential relaxation processes. It is made up of *N* Maxwell elements that are arranged in parallel. For the frequency dependence of *G'* and *G''* we find

$$G'(\omega) = \sum_{i=0}^{N} g_i \frac{\tau_i^2 \omega^2}{1+\tau_i^2 \omega^2} \tag{14}$$

$$G''(\omega) = \sum_{i=0}^{N} g_i \frac{\tau_i \omega}{1+\tau_i \omega^2} \tag{15}$$

where τ_i and g_i are the relaxation time and relaxation strength of the *i*-th mode. To avoid overfitting and to achieve comparability between the fit results, we fix the number of modes to 4. The fits of *G'* and *G''* are shown as full and broken lines, respectively, in Figure 6a, and the determined relaxation times and strengths in Figure 6b. The behavior at high frequencies corresponds to processes taking place in a short time and vice versa. Looking at the relaxation time spectra in Figure 6b, it is clear that the slower dynamics are much more affected than the faster dynamics. A stronger gel character, such as in the undecorated and Man-, Lac- as well as SiaGal-decorated peptide samples, is clearly associated with an increase in the relaxation strength of the slowest two relaxation modes and an increase of the relaxation times. This indicates the presence of a slower dynamical process taking place in the case of the gel samples, most likely on a larger length scale. The faster dynamical processes taking place on a more local scale remain largely unaffected.

When studying hydrogels, one important quantity to be discussed is the mesh size **ξ**, which is the average distance between crosslinking points in a network structure.[56] While this quantity is not accessible experimentally, we can estimate it from the plateau modulus G_0, which is the value of *G'* at the high-frequency plateau. According to classical rubber elasticity theory[57–59], the plateau modulus G_0 can be related to the number density of effective crosslinking points and therefore to a corresponding mesh size **ξ** (sometimes also referred to as the elastic blob[56]) in a hydrogel by

$$G_0 = \frac{kT}{\xi^3} \tag{16}$$

where *k* is the Boltzmann constant and *T* is the temperature in K. For our case, we take the plateau modulus to be equal to the value of the storage modulus at the highest measured frequency, $G_0 = G'(\omega = 52.4\ \text{rad/s})$. For some samples, a slope is observed at this frequency instead of a true plateau, so the determined values of G_0 and the derived **ξ** only serve as rough estimates. In general, a larger plateau modulus is associated with a smaller mesh size. Accordingly, we find that the mesh size is the smallest for the undecorated peptide at 53.1 nm and increases to up to 83.4 nm for the galactose-decorated peptide. All mesh sizes are shown in Table 1.

Additionally, continuous shear experiments were performed. The shear rate was first increased from 0.01 to 100 s^{-1} (up-sweep) and then decreased (down-sweep) to check for hysteresis effects. The results are shown in Figure 5.

All samples show shear-thinning behavior. The undecorated peptide, as well as the Lac- and SiaGal-decorated peptides, show a

TABLE 1 Results for the mesh size ξ of different 0.5% (w/v) peptide hydrogels at pH 4 and 37°C as determined from macrorheology using the value of G' at $\omega = 52.4$ rad/s.

Sample	G_0/Pa	ξ/nm
Undecorated	27.5	53.1
-Gal	7.1	83.4
-Glc	7.6	81.4
-Man	23.0	56.4
-Lac	21.7	57.5
-SiaGal	14.0	66.5

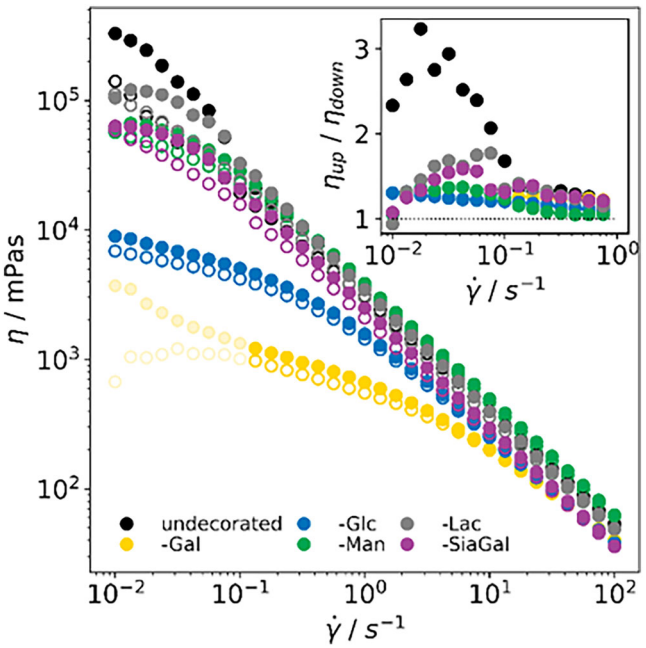

FIGURE 7 Results of continuous shear experiments performed on 0.5% (w/v) peptide hydrogels at pH 4 and 37°C. The up- and down-sweep data points are shown with filled and open circles, respectively. Since significant effects of hysteresis were detected, the ratios between the up- and down-sweeps are shown in the inset. For the very low viscous galactose-decorated samples, an unrealistic decrease of the viscosity was detected in the down sweep at low shear rates. In this case, only the data points above 0.1 s^{-1} were considered for the inset. The remaining data points are shown in a lower saturated yellow.

significantly higher viscosity at low shear rates than the Gal- and Glc-decorated variants. In addition, there are hysteresis effects, which are quantified by the ratios between the up- and down-sweep data sets, which are shown in the inset in Figure 7. In the case of the undecorated sample, the viscosity determined in the up-sweep at low shear rates is up to three times larger than in the down-sweep. The largest differences are seen for shear rates below 0.1 s^{-1}. The presence of hysteresis could indicate the existence of a (self-assembled) superstructure that is destroyed upon strong shearing and not fully reformed within the time frame of the experiment, which in our case

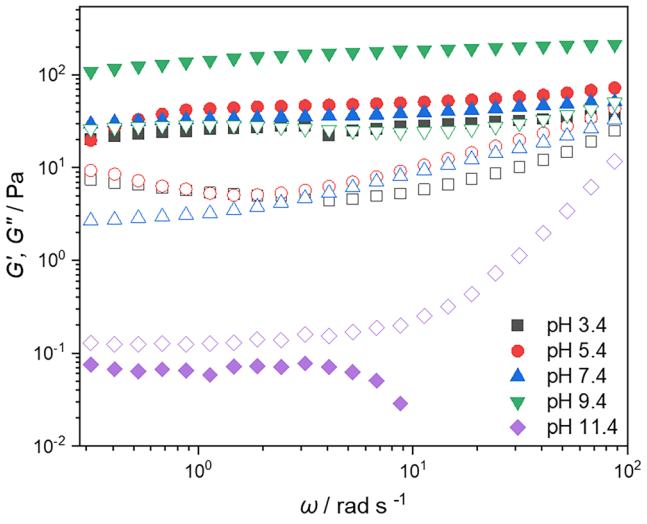

FIGURE 8 Frequency sweep data (filled symbols: G', open symbols: G'') of 0.5% (w/v) hFF03 at different pH. Samples were prepared in water + 150 mM NaCl and pH adjusted using 1 M NaOH and HCl, measured at 37°C.

was between 4.6 min for the SiaGal- and 20.9 min for undecorated sample (see Section 2.4.1). In any case, the presence of the hysteresis effects demonstrates that self-healing of the hydrogel structure in these systems requires substantial time (longer than the experiment time), and this effect is more strongly observed for the undecorated sample.

To check for the influence of pH, macrorheology was performed on the undecorated hFF03 peptide at different pH values between 3.4 and 11.4. As can be seen from Figure 8, at all probed pH values except for pH 11.4, the peptide shows typical gel behavior, with G' dominating G'' over the whole frequency range and the moduli being virtually independent of frequency.[52] At pH 11.4, the sample behaves liquid-like since G' < G''. It is safe to assume that at this point the electrostatic interactions between N- and C-termini collapse because the N-terminal amino group of *ortho*-aminobenzoic acid ($pK_a \sim 11.8$[60]) is no longer protonated and therefore uncharged. Approaching pH 10, the sample briefly became turbid, indicating limited peptide solubility at the isoelectric point (pI ∼ 10.3), before turning clear again at pH > 11.

When comparing the effective rheological mesh sizes (Table 2), it can be seen that the values at pH 3.4, 5.4, and 7.4 are largely similar (40.6-49.7 nm), while at pH 9.4 a smaller mesh size of 27.5 nm is found. This corresponds to the highest measured elastic response, making it the "stiffest" of all investigated hydrogels.

Overall, the pH-dependent experiments showed that the peptide backbone robustly forms hydrogels across a large and mucus-relevant pH-range.[61]

To investigate the influence of pH value on glycan-decorated peptides, macrorheology was carried out at pH 7.4. The frequency sweep data is shown in Figure 9. The overall curve shape for the elastic response is very similar to pH 4. The storage modulus G' is larger than the loss modulus G'' for all hydrogels. In contrast to the behavior

TABLE 2 Results for the mesh size ξ of 0.5% (w/v) undecorated hFF03 peptide at different pH and 37°C as determined from macrorheology using the value of G' at $\omega = 52.4$ rad/s.

Sample	G_0/Pa	ξ/nm
pH 3.4	34.9	49.7
pH 5.4	63.9	40.6
pH 7.4	48.5	44.5
pH 9.4	207.1	27.5
pH 11.4	no hydrogel	

TABLE 3 Results for the mesh size ξ of different 0.5% (w/v) peptide hydrogels at pH 7.4 as determined from macrorheology using the value of G' at $\omega = 52.4$ rad/s.

Sample	G_0/Pa	ξ/nm
Undecorated	49.4	44.3
-Gal	91.9	36.0
-Glc	87.6	36.6
-Man	89.1	36.4
-SiaGal	38.0	48.3

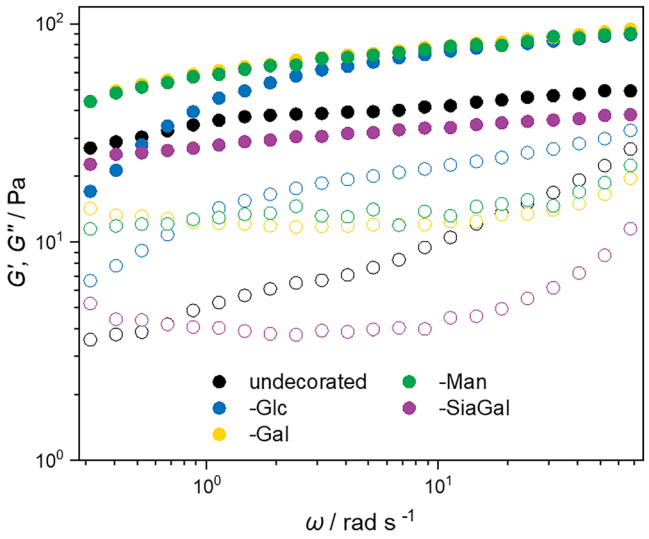

FIGURE 9 Frequency sweep data (filled symbols: G', open symbols: G'') for undecorated and decorated peptides at pH 7.4. Samples were prepared at 0.5% (w/v) in DPBS, pH adjusted to 7.4 using 1 M NaOH, and measured at 37°C.

at pH 4 (Figure 6a), the influence of glycan decoration seems to follow a different pattern here. While the samples decorated with monosaccharides (Glc, Gal, Man) show very similar behavior among each other, their viscoelastic response being higher than the undecorated peptide, the viscoelastic response of the disaccharide-decorated SiaGal-peptide is weaker as compared to the undecorated peptide.

Comparing the plateau modulus G_0 and the derived mesh size ξ at pH 4 (Table 1) and pH 7.4 (Table 3), all hydrogels are stiffer at pH 7.4, as shown by an increase in G_0 (and corresponding decrease in mesh size). However, this increase is of different magnitudes depending on the decoration. While the monosaccharide-decorated peptides show the largest increase (more than 10-fold for Gal and Glc, more than 4-fold for Man), it is less pronounced for the disaccharide-decorated SiaGal-peptide (2.7-fold) and least for the undecorated peptide (1.6-fold). Overall, this leads to a different trend at pH 7.4. The "stiffest" hydrogels are the monosaccharide-decorated ones, followed by the undecorated and the disaccharide-decorated peptide hydrogel.

In summary, from the macrorheology experiments, it is clear that the choice of glycan has a measurable effect on the viscoelastic properties of the peptide hydrogels. However, this effect varies between different pH values, and when it comes to magnitude, pH effects can exceed glycan effects. pH-dependent viscoelastic properties are also found in many native or reconstituted mucus hydrogels.[61,62] Analysis with the generalized Maxwell model shows that samples with gel-character exhibit a slower dynamical process. They also exhibit mucus-like shear-thinning behavior[62] and hysteresis in steady shear experiments, indicative of a self-assembled superstructure. When comparing the hFF03 hydrogels to other reported peptide hydrogels, G_0 at 0.5% (w/v) as a measure of gel strength is two orders of magnitude smaller than for the Fmoc-FF motif[63] and almost four orders of magnitude smaller than for some of the GxG series[64]. The MAX series (MAX8 peptide[65]) exhibits a G_0 that is 3-fold larger than that of hFF03-based gels. This is not surprising since hFF03 differs significantly from those regarding design principle, structure, and thus assembly mechanism. On the other hand, a comparison with structurally related coiled-coil-based hydrogels shows that their viscoelastic properties are also commonly tuneable over a wide range (10^0–10^4 Pa) with stimuli such as temperature[66], pH[67], or concentration[46]. The hFF03-based systems do not reach G_0 values above 200 Pa at the investigated concentration of 0.5% (w/v), but one can conclude that one of the main properties, tuneability, is well in line with reported findings on coiled-coil peptide hydrogels.

3.6.2 | Microrheology

For dynamic light scattering (DLS), microrheology tracer particles were added to the samples in the gel formation process. By scattering measurements, their mean squared displacement (MSD) and subsequently storage (G') and loss modulus (G'') can be determined. The MSD of the peptide hydrogels is shown in Figure 10a.

At very short lag times ($\tau < 10^{-4}$ s) the MSD is proportional to τ, indicating diffusive motion, characterized by the zero-shear viscosities of the solvent.[68] At intermediate lag times ($\tau > 10^{-4}$ s), the tracer particles undergo subdiffusive motion, i.e., MSD $\sim \tau^{\alpha}$, where $0 < \alpha < 1$. The time dependence of $\alpha(\omega = \tau^{-1})$ contains information about the viscoelastic properties of the sample. For the diffusive region at short lag times, we perform linear fits of the first 10 data points and obtain the associated diffusion coefficients, since $\langle \Delta r^2 \rangle = 6D\tau$ for diffusive motion in 3D. From the diffusion coefficients, we can calculate the viscosity using the Stokes-Einstein equation

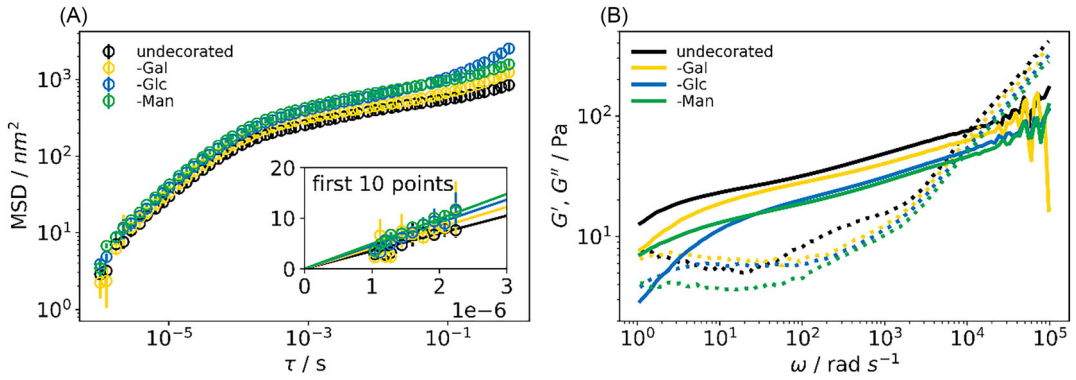

FIGURE 10 a) MSDs of peptide hydrogels as determined by DLS measurements. The point density was decreased for better lucidity. The insets show linear fits to the first 10 data points, which yield the zero-shear viscosity of the solvent. b) Results for G' (full lines) and G' (dotted lines) from DLS microrheology. Experimental conditions: 0.5% (w/v) peptide in DPBS at pH 4, 25°C.

$$\eta = \frac{kT}{6\pi RD} \tag{17}$$

where $R = 96.0$ nm is the tracer particle radius.

The diffusion coefficients, viscosities, and mesh sizes are summarized in Table 4. When looking at the mesh sizes obtained from microrheology, they all lie between 53.0 and 74.0 nm, which is consistent with the values obtained from macrorheology (53.1–81.4 nm, Table 1). However, again, different trends can be found.

The determined solvent viscosities are significantly larger than those of DPBS buffer (0.9041 mPas), indicating that the local movement of the tracer particles is sensitive to the presence of the peptide-glycan chains. Overall, we have demonstrated that DLS microrheology is a viable technique to determine the viscoelastic properties of peptide hydrogels over a wide frequency range, reducing the necessary sample volume to around ~50 µl. There is generally good agreement between macro- and microrheology, although the precise values for G_0 are slightly different between the two techniques. The local solvent viscosity around the tracer particles is significantly larger than that of the pure solvent.

TABLE 4 Diffusion coefficient and viscosity of 0.5% (w/v) peptide hydrogels at pH 4 as determined from microrheology using linear fitting of the short lag time behavior of the MSD. Results for the mesh size ξ were determined from the value of G' at $\omega = 52.4$ rad/s.

Sample	D/nm² s^{-1}	η/mPas	G_0/Pa	ξ/nm
Undecorated	(5.83 ± 0.30) × 10^5	3.45 ± 0.18	28.8	53.0
-Gal	(6.78 ± 0.64) × 10^5	2.97 ± 0.28	25.6	55.1
-Glc	(7.58 ± 0.33) × 10^5	2.66 ± 0.12	18.0	62.0
-Man	(8.21 ± 0.23) × 10^5	2.45 ± 0.07	17.1	63.0

3.6.3 | Nanorheology

Cy3 viscosity calibration and hFF03 hydrogel formation kinetics

Cyanine 3 (Cy3) belongs to the class of so-called fluorescent molecular rotors (FMRs) that have emerged as novel nanoprobes for dynamic and spatially resolved nanoviscosity sensing.[30] We recently established a Cy3 dye as a fluorescent molecular rotor for membrane nanoviscosity measurements and extensively characterized the fluorescence characteristics of Cy3 as a function of temperature and viscosity.[30] Nanoviscosity is the apparent viscosity sensed by a small molecular probe on the nanoscale in complex liquids/gels.[69,70] The excited state lifetime of Cy3 (ICC) in aqueous solution is very short ($\tau \sim 0.14$–0.18 ns[71–73]) due to a highly efficient rotation (twisting motion) around the C-C bond of the ICC methine-linker.[74] When bond rotation is hindered, either by friction with solvent molecules (viscosity) or by steric hindering, e.g., through binding to biomolecules, the radiative pathway becomes populated, generating fluorescence.[73,75–77]

Here, we use the fluorescent molecular rotor (FMR) dye Cy3 as a nanoviscosity probe to directly measure the viscosity within a 0.5% (w/v) hFF03 peptide hydrogel at pH 4 and 25°C (Figure 11). A calibration curve connects the mean fluorescence lifetime of Cy3 (τ_{mean}) to the known bulk viscosity of a buffer/sucrose mixture (Figure 11a).

Using this viscosity calibration curve, we analyzed the nanoviscosity of hFF03 at different time points in a 24 h time window after adding DPBS to the hFF03 peptide. Three gelation experiments were performed, yielding a mean nanoviscosity value of 2.0 ± 0.3 mPas for 0.5% (w/v) hFF03 at 25°C, to which the various experiments were normalized. A fit of the kinetics with an exponential function results in a time constant of ~ 2 h for gel formation based on the temporal development of the nanoviscosity, indicating that the gel formation process is safely completed after 10 h (Figure 11c). For all rheology experiments, the samples were incubated for 16–24 h before measurement.

Nanoviscosity of glycan-decorated hFF03

Next, we evaluated the Cy3 fluorescence decay curves in the different glycan-decorated hFF03 peptide hydrogels at 0.5% (w/v) and pH 4, as shown in Figure 12a. The mean lifetimes and corresponding

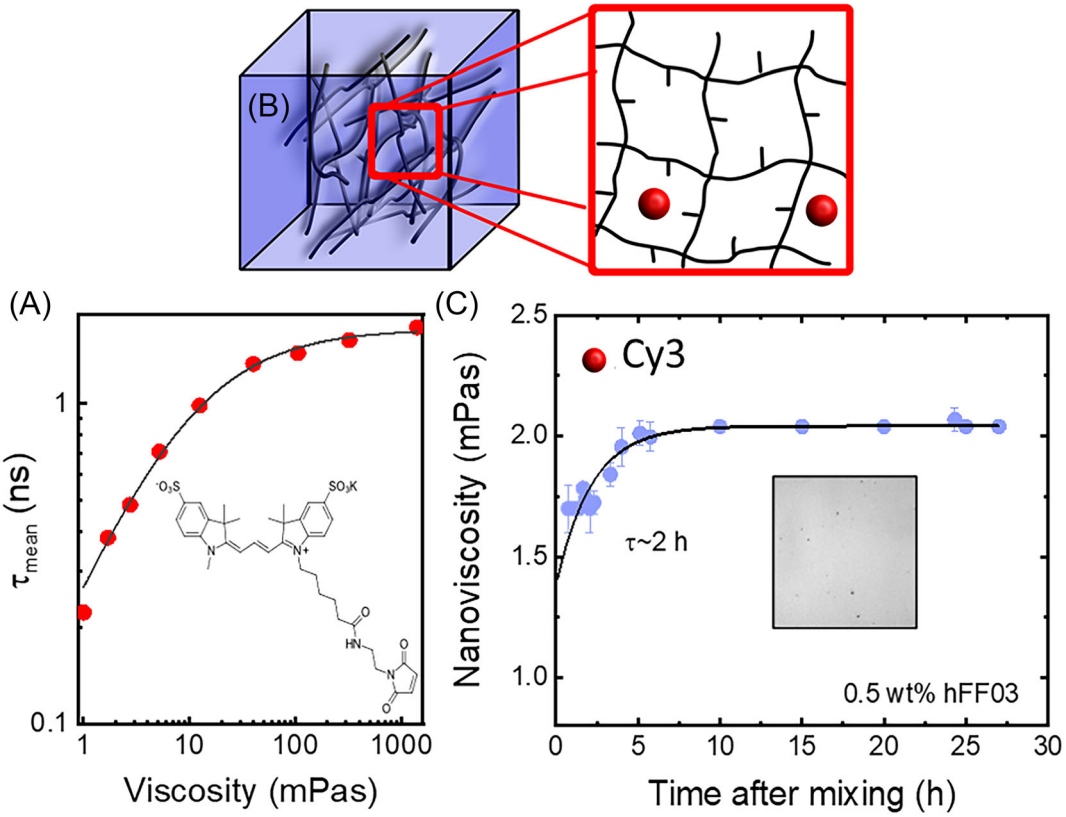

FIGURE 11 (a) Viscosity calibration curve fitted with a modified Förster-Hoffmann equation (equation 15). The chemical structure of Cy3 (sulfated cyanine 3 maleimide) is shown in the inset. b) Schematic of nanoviscosity measurement design using Cy3. c) Changes of nanoviscosity as a function of gel formation time and a monoexponential fit to the data. The time constant τ for gel formation is indicated. An initial viscosity of the aqueous hFF03 mixture at t = 0 is extrapolated from the fit with 1.138 mPas. The inset shows the image from the FLIM measurement indicative of homogeneous Cy3 nanoviscosity sensor distribution. Experimental conditions: 0.5 μM Cy3 in DPBS/sucrose mixtures, respectively, in 0.5% (w/v) hFF03, 25°C.

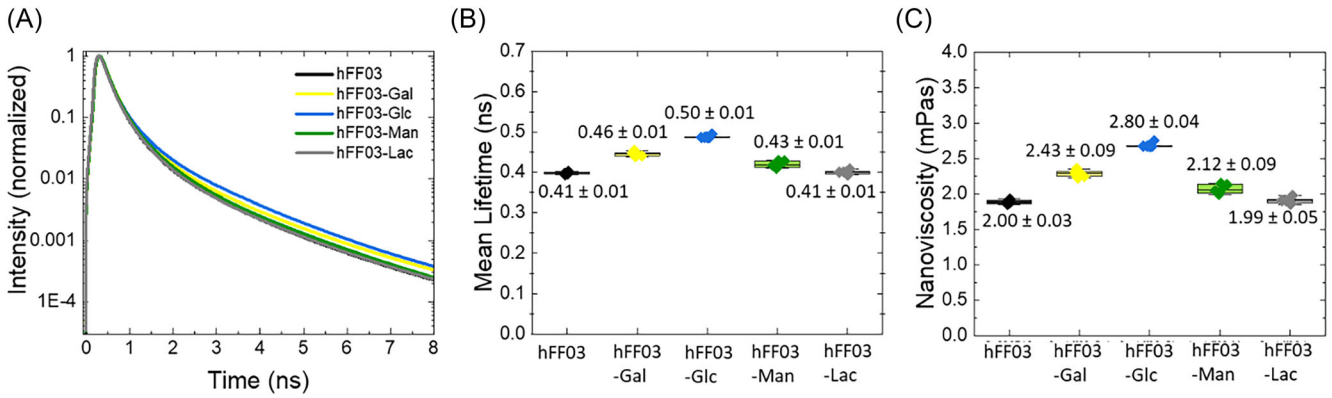

FIGURE 12 Nanoviscosity of glycan-decorated hFF03 peptide hydrogels. a) Cy3 fluorescence decay curves in the different peptide hydrogels. b) Mean fluorescence lifetimes. c) Nanoviscosity of the sugar-decorated peptides with galactose (Gal), glucose (Glu), mannose (Man), and lactose (Lac). hFF03 is shown for comparison. Experimental conditions: 0.5 μM Cy3 in 0.5% (w/v) hFF03, 25°C. For each nanoviscosity value, 4–6 measurements were performed and analyzed.

viscosity values are shown in Figure 12b and c. All nanoviscosity values range between 2 and 3 mPas (Table 5), clearly above the value for pure buffer (0.904 mPas).

Overall, they are very similar to the solution viscosity data determined using DLS (Table 4), with values between 2.5 and 3.5 mPas. However, different trends are found. While the most viscous gel as

per DLS was formed by the undecorated hFF03 peptide, here it seemed to be the glucose-decorated sample, followed by galactose and mannose. This seems to reflect the order found by macrorheology at pH 7.4 (Table 3). A possible explanation is that the determination of nanoviscosity is more susceptible to slight variations in peptide concentration, pH value, or salt content, which might lead to significant deviations here, possibly exceeding the glycan influence.

From Nano- to micro- to macrorheology

For two selected samples, undecorated hFF03 and hFF03-Man, a direct comparison was made for the nano, micro, and macrorheology measurements. Measurements were performed on aliquots of the same sample (0.5% (w/v), pH 4, 25°C) on the same day using Cy3 time-resolved fluorescence nanorheology, DLS microrheology, and macrorheology.

In Figure 13a, the MSD traces from nanoviscosity and microviscosity experiments are compared. A direct comparison between data obtained from the Cy3 fluorescence and DLS measurements is possible at very short times, for which MSD $\sim \tau$, thus indicating a diffusive motion in the solvent. The solvent viscosity values resulting from the nanoviscosity measurements are lower than those obtained from DLS, as illustrated by the steeper slope of the MSD plot (Figure 13a). The inset shows a zoom of this time window with a linear fit for the first 10 data points of the DLS measurements, yielding the solvent viscosity for the undecorated peptide at 3.45 ± 0.18 mPas and for the mannose-decorated peptide with 2.45 ± 0.07 mPas. The corresponding value obtained from nanoviscosity is 1.80 ± 0.05 mPas for both undecorated and Man-peptide.

We interpret the values such that the nanoviscosity gives the bulk solvent viscosity, while the DLS analysis yields the viscosity of an interfacial layer of solvent around the particle, which would be slightly increased in comparison to the bulk. Netz et al found evidence for the formation of an interfacial water layer with an increased water viscosity using nonequilibrium molecular dynamics simulations.[78] We are currently investigating the applicability of this concept to tracer particles in DLS microrheology as well as a combination of tracer particle-based MSD and tracer-bound FMR-based nanoviscosity determination.

For the comparison between micro- and macrorheology, the results are shown in Figure 13b using symbols. In general, there is good agreement between the two methods in the overlapping frequency range for the storage modulus *G'*. The loss modulus *G"* determined by microrheology tends to be somewhat smaller than that determined by macrorheology. The frequency dependence of *G'* and *G"* in the high-frequency regime is markedly different. *G'* shows a slow increase with a rather constant power law exponent of around 0.17. For frequencies below 10^3 rad/s *G"* is smaller than *G'* and decreases only slowly but shows a strong increase at high frequencies.

Overall, the comparison of the three rheology techniques shows that, although they focus on very different length scales, they can be combined to give a complete and consistent picture of the described hydrogels.

TABLE 5 Nanoviscosities of undecorated and glycan-decorated hFF03 at 0.5% (w/v), pH 4, and 25 °C as determined from fluorescence lifetime spectroscopy using the Cy3 viscosity calibration and the modified Förster-Hoffmann equation.

Sample	η (mPas)
Undecorated	2.00 ± 0.03
-Gal	2.49 ± 0.09
-Glc	2.80 ± 0.04
-Man	2.12 ± 0.09
-Lac	1.99 ± 0.05

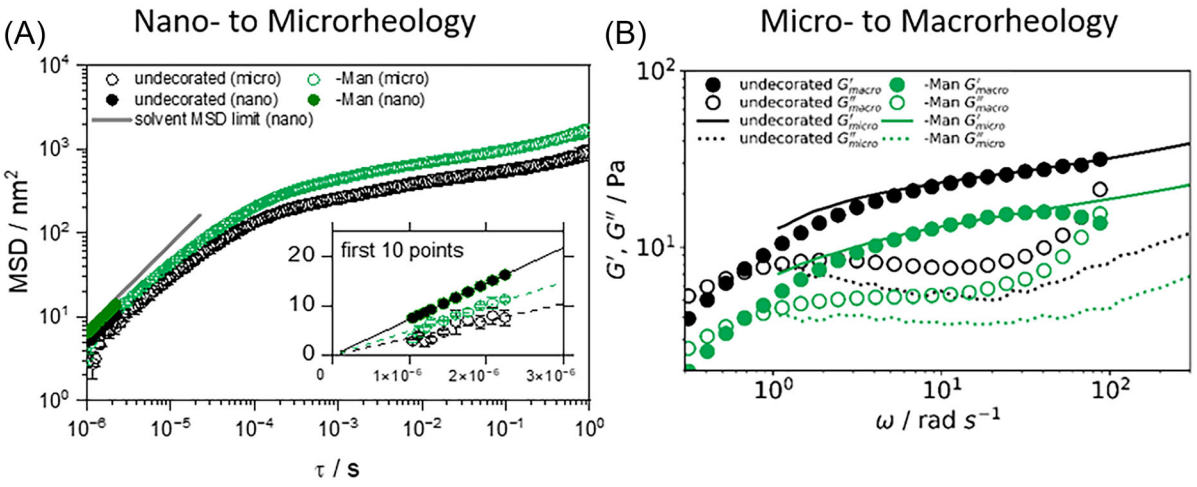

FIGURE 13 Direct comparison of nano, micro, macroviscosity data of two selected samples from which aliquots were measured on the same day with Cy3 fluorescence, DLS, and macrorheology, respectively. The comparison between MSDs calculated from the Cy3 time-resolved fluorescence (nanoviscosity) and from DLS measurements (microrheology) is shown in a). The comparison between the same DLS data and macrorheology experiments is shown in b), where *G'* and *G"* are given by the filled and open symbols respectively. Experimental conditions: 0.5% (w/v), pH 4, 25°C.

4 | CONCLUSION

In this study, we presented a simple peptide-based model for some key properties of mucus, i.e., viscoelastic behavior and the presentation of defined carbohydrate moieties. We used three complementary rheology techniques to gain an understanding of the hydrogels across all relevant length scales.

On the one hand, we found the hydrogel structure to be profoundly robust toward glycan decoration. The secondary structure was not perturbed by the introduction of glycans, as shown by CD spectroscopy. Cryo-TEM showed that fiber morphology was the same for Man- and SiaGal-decorated gels, as well as comparable to undecorated peptides. All samples that were investigated at physiologic pH formed self-supporting hydrogels with elastic moduli in the range between 38 and 90 Pa.

On the other hand, we found differences in the viscoelastic behavior depending on glycan decoration and pH value. This behavior cannot be rationalized solely by the structural findings. Therefore, we think that the differences must be based on dynamic processes. CD spectroscopy does not show this behavior because spectra are accumulated over several minutes and therefore only depict an ensemble average. The arrested cryo-state cannot reflect this behavior either. However, MD simulations of the undecorated hFF03 show that fibrils are highly dynamic and rearranged on the nanosecond timescale. Oligomers and eventually fibrils are formed via a salt-bridge network between the C- and the N-terminus of consecutive coiled coils. The oligomers can rearrange by forming Y-junctions, from which a short segment can dissociate.[49] The differently decorated peptides might differ in the speed of rearrangement and the efficiency with which the fibril network accommodates the shear strain. Specifically, due to the long and flexible linker, the glycan can form an interaction with the C-terminus of its coiled-coil peptide, thereby competing with the self-assembly of two coiled-coils dimers into an oligomer. Thus, rheological data shows more variety between different glycans than the more "static" methods such as CD and cryo-TEM.

The advantage of this peptide hydrogel clearly lies in its versatility. While it is difficult to quantify the influence of one glycan across different pH and methods, it is clear that viscoelastic properties can be tuned to match desired mucus properties. Therefore, this peptide hydrogel could be used to study more applied questions, such as pathogen interaction with mucus-derived glycans, within a hydrogel context. To bring the model system closer to the very intricate native mucus, it would be interesting to gradually increase the complexity of the system, for example, by adding more copies of complex glycans.

ACKNOWLEDGMENTS

The authors gratefully acknowledge funding by the Deutsche Forschungsgemeinschaft (DFG) through the collaborative research centre 1449 "Dynamic Hydrogels at Biointerfaces" (Project ID 431232613) and the core facility BioSupraMol. Furthermore, the authors would like to thank the HPC Service of ZEDAT, Freie Universität Berlin, for computing time.[39] MD and MCSDC thank the Max Planck Society for financial support. Open Access funding enabled and organized by Projekt DEAL.

CONFLICT OF INTEREST STATEMENT

There are no conflicts to declare.

ORCID

Jonas Proksch https://orcid.org/0009-0005-7742-7824
Beate Koksch https://orcid.org/0000-0002-9747-0740

REFERENCES

1. Wagner CE, Wheeler KM, Ribbeck K. Mucins and their role in shaping the functions of mucus barriers. *Annu Rev Cell Dev Biol*. 2018;34(1):189-215. doi:10.1146/annurev-cellbio-100617-062818
2. Wang BX, Wu CM, Ribbeck K. Home, sweet home: how mucus accommodates our microbiota. *FEBS j*. 2021;288(6):1789-1799. doi:10.1111/febs.15504
3. Bansil R, Turner BS. Mucin structure, aggregation, physiological functions and biomedical applications. *Curr Opin Colloid Interface Sci*. 2006;11(2-3):164-170. doi:10.1016/j.cocis.2005.11.001
4. Leal J, Smyth HDC, Ghosh D. Physicochemical properties of mucus and their impact on transmucosal drug delivery. *Int J Pharm*. 2017;532(1):555-572. doi:10.1016/j.ijpharm.2017.09.018
5. Wang BX, Takagi J, McShane A, et al. Host-derived O-glycans inhibit toxigenic conversion by a virulence-encoding phage in vibrio cholerae. *EMBO j*. 2023;42(3):e111562. doi:10.15252/embj.2022111562
6. Bej R, Haag R. Mucus-inspired dynamic hydrogels: synthesis and future perspectives. *J Am Chem Soc*. 2022;144(44):20137-20152. doi:10.1021/jacs.1c13547
7. Lai SK, Wang Y-Y, Wirtz D, Hanes J. Micro- and macrorheology of mucus. *Adv Drug Deliv Rev*. 2009;61(2):86-100. doi:10.1016/j.addr.2008.09.012
8. Kočevar-Nared J, Kristl J, Šmid-Korbar J. Comparative rheological investigation of crude gastric mucin and natural gastric mucus. *Biomaterials*. 1997;18(9):677-681. doi:10.1016/S0142-9612(96)00180-9
9. Wagner CE, Krupkin M, Smith-Dupont KB, et al. Comparison of physicochemical properties of native mucus and reconstituted mucin gels. *Biomacromolecules*. 2023;24(2):628-639. doi:10.1021/acs.biomac.2c01016
10. Sharma A, Thongrom B, Bhatia S, et al. Polyglycerol-based mucus-inspired hydrogels. *Macromol Rapid Commun*. 2021;42(20):2100303. doi:10.1002/marc.202100303
11. Detwiler RE, Kramer JR. Preparation and applications of artificial mucins in biomedicine. *Curr Opin Solid State Mater Sci*. 2022;26(6):101031. doi:10.1016/j.cossms.2022.101031
12. Brahmachari S, Arnon ZA, Frydman-Marom A, Gazit E, Adler-Abramovich L. Diphenylalanine as a reductionist model for the mechanistic characterization of β-amyloid modulators. *ACS Nano*. 2017;11(6):5960-5969. doi:10.1021/acsnano.7b01662
13. Diaferia C, Schiattarella C, Gallo E, et al. Fluorescence emission of self-assembling amyloid-like peptides: solution versus solid state. *ChemPhysChem*. 2021;22(21):2215-2221. doi:10.1002/cphc.202100570
14. Zacco E, Hütter J, Heier JL, et al. Tailored presentation of carbohydrates on a coiled coil-based scaffold for asialoglycoprotein receptor targeting. *ACS Chem Biol*. 2015;10(9):2065-2072. doi:10.1021/acschembio.5b00435
15. Zacco E, Anish C, Martin CE, et al. A self-assembling peptide scaffold for the multivalent presentation of antigens. *Biomacromolecules*. 2015;16(7):2188-2197. doi:10.1021/acs.biomac.5b00572

16. Hellmund KS, von Lospichl B, Böttcher C, et al. Functionalized peptide hydrogels as tunable extracellular matrix mimics for biological applications. *Peptide Sci*. 2021;113(2):e24201. doi:10.1002/pep2.24201
17. Dal Colle MCS, Ricardo MG, Hribernik N, Danglad-Flores J, Seeberger PH, Delbianco M. Linker, loading, and reaction scale influence automated glycan assembly. *Beilstein J Org Chem*. 2023;19:1015-1020. doi:10.3762/bjoc.19.77
18. Guberman M, Bräutigam M, Seeberger PH. Automated glycan assembly of Lewis type I and II oligosaccharide antigens. *Chem Sci*. 2019;10(21):5634-5640. doi:10.1039/C9SC00768G
19. Wendeln C, Heile A, Arlinghaus HF, Ravoo BJ. Carbohydrate microarrays by microcontact printing. *Langmuir*. 2010;26(7):4933-4940. doi:10.1021/la903569v
20. Patel MK, Vijayakrishnan B, Koeppe JR, Chalker JM, Doores KJ, Davis BG. Analysis of the dispersity in carbohydrate loading of synthetic glycoproteins using MALDI-TOF mass spectrometry. *Chem Commun*. 2010;46(48):9119-9121. doi:10.1039/C0CC03420G
21. Tsai T-W, Fang J-L, Liang C-Y, et al. Exploring the synthetic application of Helicobacter pylori α1,3/4-fucosyltransferase FucTIII toward the syntheses of fucosylated human milk glycans and Lewis antigens. *ACS Catal*. 2019;9(12):10712-10720. doi:10.1021/acscatal.9b03752
22. Chiu CPC, Lairson LL, Gilbert M, Wakarchuk WW, Withers SG, Strynadka NCJ. Structural analysis of the α-2,3-sialyltransferase Cst-I from campylobacter jejuni in Apo and substrate-analogue bound forms. *Biochemistry*. 2007;46(24):7196-7204. doi:10.1021/bi602543d
23. Cai PC, Krajina BA, Kratochvil MJ, et al. Dynamic light scattering microrheology for soft and living materials. *Soft Matter*. 2021;17(7):1929-1939. doi:10.1039/D0SM01597K
24. Ferreira D, Bachelard R, Guerin W, Kaiser R, Fouché M. Connecting field and intensity correlations: the Siegert relation and how to test it. *Am J Physiol*. 2020;88(10):831-837. doi:10.1119/10.0001630
25. Siegert AJF, Massachusetts Institute of Technology Radiation, L. *On the fluctuations in signals returned by many independently moving scatterers*. Radiation Laboratory, Massachusetts Institute of Technology [Cambridge, Mass.]; 1943.
26. Mason TG, Gang H, Weitz DA. Rheology of complex fluids measured by dynamic light scattering. *J Mol Struct*. 1996;383(1-3):81-90. doi:10.1016/S0022-2860(96)09272-1
27. Mason TG, Weitz DA. Optical measurements of frequency-dependent linear viscoelastic moduli of complex fluids. *Phys Rev Lett*. 1995;74(7):1250-1253. doi:10.1103/PhysRevLett.74.1250
28. Mason TG. Estimating the viscoelastic moduli of complex fluids using the generalized Stokes–Einstein equation. *Rheol Acta*. 2000;39:371-378. doi:10.1007/s003970000094
29. Mason TG, Ganesan K, van Zanten JH, Wirtz D, Kuo SC. Particle tracking microrheology of complex fluids. *Phys Rev Lett*. 1997;79(17):3282-3285. doi:10.1103/PhysRevLett.79.3282
30. Ober K, Volz-Rakebrand P, Stellmacher J, et al. Expanding the scope of reporting nanoparticles: sensing of lipid phase transitions and nanoviscosities in lipid membranes. *Langmuir*. 2019;35(35):11422-11434. doi:10.1021/acs.langmuir.9b01372
31. Volz P, Brodwolf R, Zoschke C, Haag R, Schäfer-Korting M, Alexiev U. White-light supercontinuum laser-based multiple wavelength excitation for TCSPC-FLIM of cutaneous nanocarrier uptake. *Z Phys Chem*. 2018;232(5-6):671-688. doi:10.1515/zpch-2017-1050
32. Alexiev U, Farrens DL. Fluorescence spectroscopy of rhodopsins: insights and approaches. *BBA-Bioenergetics*. 2014;1837(5):694-709. doi:10.1016/j.bbabio.2013.10.008
33. Kim TY, Winkler K, Alexiev U. Picosecond multidimensional fluorescence spectroscopy: a tool to measure real-time protein dynamics during function. *Photochem Photobiol*. 2007;83(2):378-384. doi:10.1562/2006-06-21-RA-943
34. Swindells JF, Synder CF, Hardy RC, Golden PE. *Viscosities of sucrose solutions at Varoius temperatures: tables of recalculated values*. Government Printing Office; 1958.
35. Vyšniauskas A, Lopez-Duarte I, Duchemin N, et al. Exploring viscosity, polarity and temperature sensitivity of BODIPY-based molecular rotors. *Phys Chem Chem Phys*. 2017;19(37):25252-25259. doi:10.1039/c7cp03571c
36. Wood CW, Woolfson DN. CCBuilder 2.0: powerful and accessible coiled-coil modeling. *Protein Sci*. 2018;27(1):103-111. doi:10.1002/pro.3279
37. Case DA, Cheatham TE III, Darden T, et al. The Amber biomolecular simulation programs. *J Comput Chem*. 2005;26(16):1668-1688. doi:10.1002/jcc.20290
38. Danne R, Poojari C, Martinez-Seara H, et al. doGlycans–tools for preparing carbohydrate structures for atomistic simulations of glycoproteins, glycolipids, and carbohydrate polymers for GROMACS. *J Chem Inf Model*. 2017;57(10):2401-2406. doi:10.1021/acs.jcim.7b00237
39. *Curta: a general-purpose high-performance computer at ZEDAT*. Freie Universität Berlin; 2020.
40. Lindorff-Larsen K, Piana S, Palmo K, et al. Improved side-chain torsion potentials for the Amber ff99SB protein force field. *Proteins: Structure Function Bioinformatics*. 2010;78(8):1950-1958. doi:10.1002/prot.22711
41. Jorgensen MD, Chmielewski J. Recent advances in coiled-coil peptide materials and their biomedical applications. *Chem Commun*. 2022;58(83):11625-11636. doi:10.1039/D2CC04434J
42. Pagel K, Koksch B. Following polypeptide folding and assembly with conformational switches. *Curr Opin Chem Biol*. 2008;12(6):730-739. doi:10.1016/j.cbpa.2008.09.005
43. Dawson WM, Martin FJO, Rhys GG, Shelley KL, Brady RL, Woolfson DN. Coiled coils 9-to-5: rational de novo design of α-helical barrels with tunable oligomeric states. *Chem Sci*. 2021;12(20):6923-6928. doi:10.1039/D1SC00460C
44. Mehrban N, Zhu B, Tamagnini F, et al. Functionalized α-helical peptide hydrogels for neural tissue engineering. *ACS Biomater Sci Eng*. 2015;1(6):431-439. doi:10.1021/acsbiomaterials.5b00051
45. Mehrban N, Abelardo E, Wasmuth A, et al. Assessing cellular response to functionalized α-helical peptide hydrogels. *Adv Healthc Mater*. 2014;3(9):1387-1391. doi:10.1002/adhm.201400065
46. Huang C-C, Ravindran S, Yin Z, George A. 3-D self-assembling leucine zipper hydrogel with tunable properties for tissue engineering. *Biomaterials*. 2014;35(20):5316-5326. doi:10.1016/j.biomaterials.2014.03.035
47. Hill LK, Meleties M, Katyal P, et al. Thermoresponsive protein-engineered coiled-coil hydrogel for sustained small molecule release. *Biomacromolecules*. 2019;20(9):3340-3351. doi:10.1021/acs.biomac.9b00107
48. Hellmund KS. *Coiled-coil based 3D scaffolds as highly specialized biological microenvironments*. Freie Universität Berlin; 2021.
49. Heinz F, Proksch J, Schmidt RF, Gradzielski M, Koksch B, Keller BG. How chromophore labels shape the structure and dynamics of a peptide hydrogel. *Biomacromolecules*. 2024;25(2):1262-1273. doi:10.1021/acs.biomac.3c01225
50. Luis AS, Hansson GC. Intestinal mucus and their glycans: a habitat for thriving microbiota. *Cell Host Microbe*. 2023;31(7):1087-1100. doi:10.1016/j.chom.2023.05.026
51. Pandya MJ, Spooner GM, Sunde M, Thorpe JR, Rodger A, Woolfson DN. Sticky-end assembly of a designed peptide fiber provides insight into protein fibrillogenesis. *Biochemistry*. 2000;39(30):8728-8734. doi:10.1021/bi000246g
52. Rubinstein M, Colby RH. *Polymer physics*. Oxford University Press; 2003. doi:10.1093/oso/9780198520597.001.0001
53. Tschoegl NW. *The phenomenological theory of linear viscoelastic behavior: an introduction*. Springer-Verlag; 1989. doi:10.1007/978-3-642-73602-5

54. Wiechert E. Gesetze der elastischen Nachwirkung für constante Temperatur. *Ann Phys*. 1893;286(11):546-570. doi:10.1002/andp.18932861110
55. Applications of Dynamics to Physics and Chemistry. *Nature*. 1888;38:585-587. doi:10.1038/038585a0
56. Tsuji Y, Li X, Shibayama M. Evaluation of mesh size in model polymer networks consisting of tetra-arm and linear poly (ethylene glycol)s. *Gels*. 2018;4(2):50. doi:10.3390/gels4020050
57. Doi M, Edwards SF. *The theory of polymer dynamics*. Clarendon Press; 1986.
58. de Gennes PG. *Scaling concepts in polymer physics*. Cornell University Press; 1979.
59. Pincus P. Excluded volume effects and stretched polymer chains. *Macromolecules*. 1976;9(3):386-388. doi:10.1021/ma60051a002
60. *CRC handbook of chemistry and physics*. 97th ed. CRC Press; 2016:2670.
61. Ruiz-Pulido G, Medina DI. An overview of gastrointestinal mucus rheology under different pH conditions and introduction to pH-dependent rheological interactions with PLGA and chitosan nanoparticles. *Eur J Pharm Biopharm*. 2021;159:123-136. doi:10.1016/j.ejpb.2020.12.013
62. Celli JP, Turner BS, Afdhal NH, et al. Rheology of gastric mucin exhibits a pH-dependent sol−gel transition. *Biomacromolecules*. 2007;8(5):1580-1586. doi:10.1021/bm0609691
63. Mahler A, Reches M, Rechter M, Cohen S, Gazit E. Rigid, self-assembled hydrogel composed of a modified aromatic dipeptide. *Adv Mater*. 2006;18(11):1365-1370. doi:10.1002/adma.200501765
64. Thursch LJ, Lima TA, O'Neill N, et al. Influence of central sidechain on self-assembly of glycine-x-glycine peptides. *Soft Matter*. 2023;19(3):394-409. doi:10.1039/D2SM01082H
65. Yan C, Altunbas A, Yucel T, Nagarkar RP, Schneider JP, Pochan DJ. Injectable solid hydrogel: mechanism of shear-thinning and immediate recovery of injectable β-hairpin peptide hydrogels. *Soft Matter*. 2010;6(20):5143-5156. doi:10.1039/C0SM00642D
66. Banwell EF, Abelardo ES, Adams DJ, et al. Rational design and application of responsive α-helical peptide hydrogels. *Nat Mater*. 2009;8(7):596-600. doi:10.1038/nmat2479
67. Fletcher NL, Lockett CV, Dexter AF. A pH-responsive coiled-coil peptide hydrogel. *Soft Matter*. 2011;7(21):10210-10218. doi:10.1039/C1SM06261A
68. Akimoto M, Hashi Y, Suzuki A. Mean squared displacement of a probe particle in a viscoelastic fluid. *AIP Conf Proc*. 2006;832:545-548. doi:10.1063/1.2204560
69. Kalwarczyk T, Ziebacz N, Bielejewska A, et al. Comparative analysis of viscosity of complex liquids and cytoplasm of mammalian cells at the nanoscale. *Nano Lett*. 2011;11(5):2157-2163. doi:10.1021/nl2008218
70. Sluch MI, Somoza MM, Berg MA. Friction on small objects and the breakdown of hydrodynamics in solution: rotation of anthracene in poly (isobutylene) from the small-molecule to polymer limits. *J Phys Chem B*. 2002;106(29):7385-7397. doi:10.1021/jp025549u
71. Boreham A, Brodwolf R, Pfaff M, et al. Temperature and environment dependent dynamic properties of a dendritic polyglycerol sulfate. *Polym Adv Technol*. 2014;25(11):1329-1336. doi:10.1002/pat.3355
72. Boreham A, Brodwolf R, Walker K, Haag R, Alexiev U. Time-resolved fluorescence spectroscopy and fluorescence lifetime imaging microscopy for characterization of dendritic polymer nanoparticles and applications in nanomedicine. *Molecules*. 2016;22(1):E17. doi:10.3390/molecules22010017
73. Boreham A, Pikkemaat J, Volz P, et al. Detecting and quantifying biomolecular interactions of a dendritic polyglycerol sulfate nanoparticle using fluorescence lifetime measurements. *Molecules*. 2015;21(1):E22. doi:10.3390/molecules21010022
74. Akesson E, Sundstrom V, Gillbro T. Solvent-dependent barrier heights of excited-state photoisomerization reactions. *Chem Phys Lett*. 1985;121(6):513-522. doi:10.1016/0009-2614(85)87132-3
75. Brodwolf R, Volz-Rakebrand P, Stellmacher J, et al. Faster, sharper, more precise: automated cluster-FLIM in preclinical testing directly identifies the intracellular fate of theranostics in live cells and tissue. *Theranostics*. 2020;10(14):6322-6336. doi:10.7150/thno.42581
76. Stennett EMS, Ciuba MA, Lin S, Levitus M, Demystifying PIFE. The photophysics behind the protein-induced fluorescence enhancement phenomenon in Cy3. *J Phys Chem Lett*. 2015;6(10):1819-1823. doi:10.1021/acs.jpclett.5b00613
77. Sundström V, Gillbro T. Excited state dynamics and photophysics of aggregated dye chromophores in solution. *J Chem Phys*. 1985;83(6):2733-2743. doi:10.1063/1.449275
78. Schlaich A, Kappler J, Netz RR. Hydration friction in nanoconfinement: from bulk via interfacial to dry friction. *Nano Lett*. 2017;17(10):5969-5976. doi:10.1021/acs.nanolett.7b02000

SUPPORTING INFORMATION

Additional supporting information can be found online in the Supporting Information section at the end of this article.

How to cite this article: Proksch J, Dal Colle MCS, Heinz F, et al. Impact of glycan nature on structure and viscoelastic properties of glycopeptide hydrogels. *J Pept Sci*. 2024;30(8):e3599. doi:10.1002/psc.3599